Journal of the Mechanics and Physics of Solids 120 (2018) 36–48

Contents lists available at ScienceDirect

Journal of the Mechanics and Physics of Solids

journal homepage: www.elsevier.com/locate/jmps

Phase field crystal modeling of grain boundary structures and growth in polycrystalline graphene

Jiaoyan Li [a], Bo Ni [a], Teng Zhang [b], Huajian Gao [a,*]

[a] School of Engineering, Brown University, Providence, RI 02912, USA
[b] Department of Mechanical and Aerospace Engineering, Syracuse University, Syracuse, NY 13244, USA

ARTICLE INFO

Article history:
Received 7 September 2017
Revised 11 December 2017
Accepted 29 December 2017
Available online 30 December 2017

Keywords:
Phase field crystal modeling
Grain boundary engineering in 2D material
Triple-junction-free polycrystalline graphene

ABSTRACT

A key challenge in large-scale graphene fabrication and application is controlling the grain boundaries (GBs) in polycrystalline graphene grown by chemical vapor deposition (CVD). Here, we adopt a phase field crystal (PFC) model to predict the equilibrium structures as well as dynamic formation of GBs in CVD-grown graphene. The results demonstrate that GBs consisting of clustered 5|7|5|7 dislocation dipoles, as constructed by the conventional coincidence site lattice (CSL) theory, are not energetically favorable, and should be replaced by dispersed 5|7 dislocations, as predicted from the PFC model, when constructing GBs' atomistic structures for theoretical and numerical investigations. The PFC modeling also demonstrates possible routes of engineering GBs in two-dimensional (2D) materials by controlling grain orientations in pre-patterned growing seeds and suggests a simple geometric rule that explains the predominant existence of curved grain boundaries in graphene. As a prominent example of potential applications of our method, we show how to grow triple-junction-free polycrystalline graphene that exhibits enhanced mechanical strength and defy the traditional Hall–Petch relation.

© 2018 Elsevier Ltd. All rights reserved.

1. Introduction

Among various promising techniques for synthesizing large-area, high-quality mono-layer graphene, chemical vapor deposition (CVD) is by far the most important one (Geng et al., 2012; Li et al., 2009). CVD-grown graphene is typically polycrystalline (Huang et al., 2011; Yazyev and Chen, 2014). The presence of grain boundaries (GBs) could substantially influence various properties of graphene, such as mechanical strength (Huang et al., 2011; Jhon et al., 2013; Wei et al., 2012), carrier mobility (Gargiulo and Yazyev, 2013; Jauregui et al., 2011; Nemes-Incze et al., 2013) and thermal conductivity (Yasaei et al., 2015). Thus, considerable experimental effort has been exerted to reduce the density of GBs (Li et al., 2011; Ma et al., 2013). However, recent studies have also shown that GBs provide a possible way to tune the properties of graphene. The mechanical strength of polycrystalline graphene varies depending on GB morphology and the density of triple junctions (TJs) (Lee et al., 2013; Shekhawat and Ritchie, 2016; Zhang et al., 2015). GB-induced phonon softening and scattering decrease thermal conductivity (Ma et al., 2017; Mortazavi et al., 2014; Serov et al., 2013) but may improve the thermoelectric efficiency of graphene (Zhang et al., 2010). Furthermore, GBs can markedly alter electronic transport (Ma et al., 2014; Tsen et al., 2012; Yazyev and Louie, 2010); two distinct transport behaviors (high transparency and perfect reflection of charge carriers) have been observed depending on the specific GB structure (Yazyev and Louie, 2010; Yin et al., 2014; Zhang and Zhao, 2013).

* Corresponding author.
E-mail address: huajian_gao@brown.edu (H. Gao).

https://doi.org/10.1016/j.jmps.2017.12.013
0022-5096/© 2018 Elsevier Ltd. All rights reserved.

These studies are calling for a systematic effort to understand equilibrium structures and dynamic formation mechanisms of GBs in CVD-grown graphene and to explore the potential for tuning the functionalities of graphene-based structures through GB engineering. The present study is a preliminary attempt in that direction.

According to scanning tunneling microscopy (STM) images, GBs in graphene are comprised of strings of pentagon-heptagon dislocations (5|7 dislocations) separating adjacent grains of different orientations (Huang et al., 2011; Rasool et al., 2014). Following the classical dislocation theory, a coincidence site lattice (CSL) approach (Bergvall et al., 2015; Carlsson et al., 2011; Wei et al., 2012) connecting Burgers vector and GB misorientation angle has been developed to construct linear, symmetric GBs with well-defined periodic arrays of dislocations, and more recently extended to model asymmetric, curved GBs (Zhang et al., 2015). Molecular dynamics (MD) has been used to build atomic structures of GBs through annealing (Liu and Yakobson, 2010; Ophus et al., 2015) or adding/deleting atoms according to some pre-selected criteria (Jung et al., 2015; Kotakoski and Meyer, 2012; Wu and Wei, 2013). However, these methods have not been able to successfully model the dynamic process of GBs formation in graphene during CVD growth, a problem of critical importance to GB engineering in 2D materials. Recently, first-principles calculations and Monte Carlo modeling have been proposed to simulate graphene growth by examining the adsorption process of carbon atoms onto metal surfaces and to explore mechanisms that could break the well-known hexagonal growth mode (Artyukhov et al., 2015). In addition, an energy-driven kinetic Monte Carlo (kMC) method has been devised to explore how an amorphous carbon system evolved into graphene domains with GBs (Zhuang et al., 2016). In spite of these progresses, there is still limited knowledge to date regarding realistic growth kinetics and rules that govern GBs formation in graphene due to a lack of effective theoretical models and also because visualization techniques in experiments are often too time-consuming to capture the dynamic process of GBs formation during CVD growth.

In recent years, phase field (PF) and phase field crystal (PFC) models have been used extensively for modeling the evolution of micro- and nanostructures, including solidification, solid-liquid transition, grain growth, interface/surface diffusion, solid state transformations, etc. (Chen, 2002; Emmerich et al., 2012; Provatas and Elder, 2011). A PF model has been proposed to describe diverse growth morphologies (dendrites, squares, stars, hexagons, butterflies, and lobes) of CVD-grown graphene on copper foils (Meca et al., 2013). Similar model has also been used to investigate the role of oxygen in the morphological evolution of graphene domains during CVD-growth, with predictions in good agreement with experimental observations (Hao et al., 2013). Despite the versatility of PF models in describing the diffusive dynamics of microstructure evolution, the absence of atomic details presents a severe limitation in capturing material properties related to the detailed atomic arrangement, such as the effects of dislocations and GBs in 2D materials.

As an extension of the phase field formalism, PFC models naturally incorporate diffusive dynamics at atomic resolution by introducing an atomically varying density field of an order parameter (Elder and Grant, 2004; Elder et al., 2002; Mkhonta et al., 2013). Such models aim to resolve systems on atomic length and diffusive time scales, and therefore lie in between standard phase field and atomistic modeling approaches. The advantage of retaining atomic-scale spatial resolution is that the underlying mechanisms associated with the evolution of disclinations, dislocations, and/or grain boundaries in polycrystalline materials can be modeled at a diffusive time scale, where a time-averaged density field is adopted to describe some emergent long-time phenomena while the fast dynamics of atomic vibration is filtered out. The original PFC model was predominantly applied to 2D triangular and 3D bcc crystals (Elder and Grant, 2004; Elder et al., 2002), and later extended to other crystal structures including fcc and hexagonal closed packed structures (Greenwood et al., 2010; Jaatinen and Ala-Nissila, 2010; Wu et al., 2010). For 2D materials with honeycomb structures, it is straightforward to relate their hexagonal atomic structure to a hexagonal pattern of density field minima while the density field maxima correspond to a 2D triangular lattice. In practice, it is also convenient to invert the density field to yield a hexagonal (triangular) lattice of density maxima (minima). An early attempt of using PFC models to study 2D materials focused on the effect of distributed defects in graphene on out-of-plane deformation and fracture toughness (Zhang et al., 2014). Recent developments have expanded the PFC models to graphene and other 2D binary systems with more complex structures and unusual topological defects. A new structural PFC model has been developed to simulate the nucleation, growth, and formation of polycrystalline graphene (Seymour and Provatas, 2016). By fitting to a quantum mechanics density functional theory, PFC models including the one-mode model, the amplitude model, the three-mode model and the structural model, have successfully predicted the formation energies and defect structures of grain boundaries in polycrystalline graphene samples (Hirvonen et al., 2016). More recently, a PFC model has been parameterized to match the ordering, symmetry, energy and length scales of binary 2D materials, e.g. hexagonal boron nitride (h-BN), and then used to reveal new dislocation core structures in various symmetrically and asymmetrically tilted grain boundaries (Taha et al., 2017). Here, we further extend the PFC approach to simulate GBs formation during the dynamic processes of grain growth and coalescence in CVD-grown graphene, with an aim to demonstrate possible routes to engineering GBs morphologies in 2D materials.

This paper is organized as follows. Section 2 reviews the standard CSL theory in constructing GBs in graphene with various misorientation angles. Section 3 is dedicated to the adopted phase field crystal (PFC) model and its numerical implementation. Section 4 compares the atomic structures of GBs predicted from the PFC model and those from the CSL theory at selected misorientation angles. Section 5 applies the developed PFC model to GBs formation in polycrystalline graphene during dynamic growth, with a prominent example demonstrating the growth of triple-junction-free polycrystalline graphene that exhibits enhanced mechanical strength and defy the traditional Hall-Petch relation, followed by some concluding remarks in Section 6.

Table 1
Indices, lengths and orientations of matching vectors for symmetric GBs under consideration.

Indices (n, m)	Length (Å)	Misorientation angle (°)
(7, 6)	27.33	5.09
(4, 3)	14.75	9.43
(3, 2)	10.57	13.17
(5, 3)	16.97	16.43
(4, 2)	12.83	21.79
(6, 2)	17.49	32.20
(8, 2)	22.22	38.21
(10, 2)	27.00	42.10
(12, 2)	31.80	44.82
(14, 2)	36.61	46.83
(20, 2)	51.10	50.57

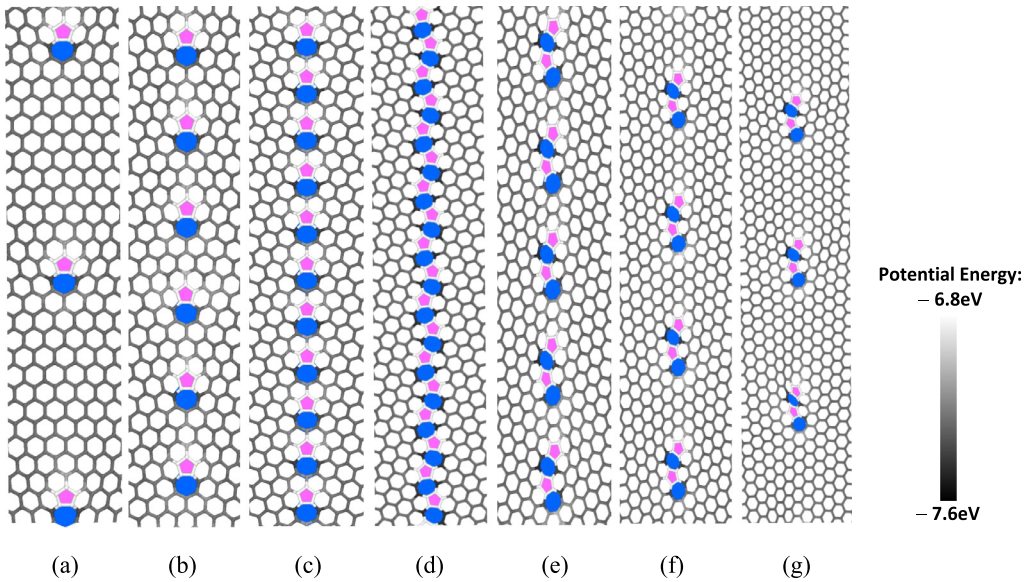

Fig. 1. Atomic structures of GBs constructed from CSL with misorientation angles of: (a) $\theta = 5.09$, (b) $\theta = 13.17$, (c) $\theta = 21.79$, (d) $\theta = 32.2$, (e) $\theta = 42.1$, (f) $\theta = 46.83$, and (g) $\theta = 50.57$.

2. Coincidence site lattice (CSL) theory

In the standard CSL theory for construction of symmetric and asymmetric GBs in 2D materials, a basic assumption is that the smoothest possible connection between two grains at a given misorientation angle is the most energetically favorable structure, typically leading to GBs with ordered and periodic atomic structures (Carlsson et al., 2011). Analogous to the standard chirality indices for carbon nanotubes, GBs in graphene can also be described by a pair of integers (n, m) according to the matching vector $\mathbf{b} = n\mathbf{a}_1 + m\mathbf{a}_2$ ($\mathbf{a}_1, \mathbf{a}_2$ are lattice vectors, and n, m are prime numbers), whose length is calculated as $d_{(n,m)} = a\sqrt{m^2 + mn + n^2}$ and the associated orientation angle as $\theta_{(n,m)} = \arcsin(|n-m|/2\sqrt{m^2 + mn + n^2})$; $a = \sqrt{3}a_0$ and $a_0 = 1.42$ Å for graphene. The indices (n, m) are not necessarily identical for the two grains adjacent to a GB, as long as the commensurability condition that the lengths of the matching vectors be equal is satisfied, i.e.,$\sqrt{{m_1}^2 + m_1 n_1 + {n_1}^2} = \sqrt{{m_2}^2 + m_2 n_2 + {n_2}^2}$. Here, we only consider symmetric GBs for which (n_1, m_1) and (n_2, m_2) are identical. Table 1 lists the indices, lengths and orientations of matching vectors for eleven cases of symmetric GBs under investigation. Due to the symmetry, the misorientation angle of a GB is just twice of the orientation angle of the corresponding matching vector.

Fig. 1 illustrates seven representative GBs among the eleven cases listed in Table 1. The color of C–C bonds scales with their potential energy after relaxation; a lighter than usual color corresponds to higher energy, which highlights pentagons, and a darker color corresponds to lower energy, which highlights heptagons. GBs constructed from the CSL theory can be classified into two categories according to the associated defect structure, one without isolated 5|7|5|7 clusters of dislocation dipoles (Fig. 1a–d) and the other with isolated 5|7|5|7 clusters (Fig. 1e–g). For the second category (GBs with misorientation angles beyond 40°), it is clearly seen that the isolated 5|7|5|7 cluster serves as a building block in the construction of GB structures.

3. PFC model and numerical implementation

In this section, we briefly discuss the adopted PFC model and its finite element (FEM) implementation. This method represents one of the latest simulation methodologies in material science, where the evolution of microstructure is described by an atomic density field according to dissipative dynamics driven by the minimization of a free energy functional.

The starting point of the PFC model is the construction of the free energy functional which was originally developed for periodic systems with spatial gradients (Elder and Grant, 2004; Elder et al., 2002) and later on proven to be equivalent to the classical density functional theory of freezing in certain limits (Elder et al., 2007). In this work, we adopt the Swift–Hohenberg free energy functional (Elder et al., 2002),

$$F = \int \left[\frac{1}{2}\phi(-\varepsilon + (q_0^2 + \nabla^2)^2)\phi + \frac{1}{4}\phi^4 \right] d\mathbf{x}, \tag{1}$$

where $\nabla = \partial/\partial x \mathbf{e}_i + \partial/\partial y \mathbf{e}_j$ is the gradient vector operator in 2D, q_0 controls the equilibrium lattice constant (taken as 1.0), ε is the reduced temperature, and ϕ is the reduced mass density. The Swift–Hohenberg functional is the simplest form that produces periodic density fields that naturally incorporate elastic/plastic lattice deformation, allow multiple grain orientations, and accommodate interfaces and free surfaces. In 2D space, minimizing the free energy functional in Eq. (1) can yield constant (ϕ_{liquid}), striped (ϕ_{strip}), and hexagonal ($\phi_{hexagonal}$) density states depending on the reduced temperature ε and the average value of the reduced mass density $\bar{\phi}$,

$$\phi_{liquid} = \bar{\phi} \tag{2}$$

$$\phi_{strip} = A_s \sin(q_s x) + \bar{\phi} \tag{3}$$

$$\phi_{hexagonal} = A_h[\cos(q_h x)\cos(q_h y/\sqrt{3}) - \cos(2q_h y/\sqrt{3})/2] + \bar{\phi} \tag{4}$$

$$q_s = q_0; A_s = 2\sqrt{\varepsilon/3 - \bar{\phi}^2} \tag{5}$$

$$q_h = \sqrt{3}q_0/2; A_h = 4(\bar{\phi} + \sqrt{15\varepsilon - 36\bar{\phi}^2}/3)/5 \tag{6}$$

For specific systems, the two adjustable parameters ε and $\bar{\phi}$ can be determined by fitting either the solid–liquid interfacial properties, mechanical properties (including effective elastic modulus, grain boundary energy density, etc.), or diffusion coefficients (Elder and Grant, 2004). In this work, the PFC model is used to produce the hexagonal structure of a 2D material, and therefore ε and $\bar{\phi}$ are taken to be 0.15 and 0.181 according to the PFC phase diagram (Galenko et al., 2013; Tang et al., 2014).

To obtain the governing equations for the density field $\phi(\mathbf{x},t)$, it is first assumed that the evolution of $\phi(\mathbf{x},t)$ is characterized by a particle current (Marconi and Tarazona, 1999),

$$\mathbf{J}(\mathbf{x},t) = -\Gamma \nabla \mu(\mathbf{x},t), \tag{7}$$

where Γ is a mobility coefficient (here taken to be 1.0) and μ the chemical potential

$$\mu = \frac{\delta F}{\delta \phi} = [-\varepsilon + (1+\nabla^2)^2]\phi + \phi^3. \tag{8}$$

Mass conservation requires

$$\frac{\partial \phi}{\partial t} + \nabla \cdot \mathbf{J}(\mathbf{x},t) = 0. \tag{9}$$

Combining Eqs. (1), (7)–(9) yields the governing equation

$$\frac{\partial \phi}{\partial t} = \nabla^2\{[-\varepsilon + (1+\nabla^2)^2]\phi + \phi^3\} \tag{10}$$

which can be solved by spectral methods in Fourier space (Hirvonen et al., 2016; Seymour and Provatas, 2016). However, numerical methods in real space, such as the finite difference and FEM methods, can provide more flexibility in handling complex geometrical shapes (Zhang et al., 2014) and enhance the computational efficiency (Salvalaglio et al., 2017). Here, we adopt the FEM approach.

Numerical schemes based on a mixed FEM formulation have been proposed by introducing new variables to reduce the order of spatial derivatives (Backofen et al., 2007). Similarly, we introduce two new variables (u, μ) together with ϕ to reduce the sixth order spatial derivatives in Eq. (10) to a set of second order partial differential equations:

$$\frac{\partial \phi}{\partial t} = \nabla^2 \mu \tag{11}$$

$$\mu = (-\varepsilon + 1)\phi + 2u + \nabla^2 u + \phi^3 \tag{12}$$

$$u = \nabla^2 \phi \tag{13}$$

In the FEM formulation, Eqs. (11)–(13) are recast in the following weak form

$$\int_\Omega \frac{\partial \phi}{\partial t} q dx = \int_\Omega (\nabla^2 \mu) q dx = \int_{\partial\Omega} \nabla\mu \cdot \mathbf{n} q d\Gamma - \int_\Omega \nabla\mu \cdot \nabla q dx \tag{14}$$

$$\begin{aligned}\int_\Omega \mu v dx &= \int_\Omega (-\varepsilon\phi + \phi) + 2u + \phi^3) v dx + \int_\Omega (\nabla^2 u) v dx \\ &= \int_\Omega (-\varepsilon + 1)\phi + 2u + \phi^3) v dx + \int_{\partial\Omega} \nabla u \cdot \mathbf{n} v dx - \int_\Omega \nabla u \cdot \nabla v dx\end{aligned} \tag{15}$$

$$\int_\Omega u w dx = \int_\Omega \nabla^2 \phi w dx = \int_{\partial\Omega} \nabla\phi \cdot \mathbf{n} w d\Gamma - \int_\Omega \nabla\phi \cdot \nabla w dx \tag{16}$$

where (q, v, w) are test functions. Under periodic boundary conditions, the surface (edge) integral terms regarding the density gradient $\nabla\phi$, the gradient of the Laplacian of the density ∇u, and the gradient of the chemical potential $\nabla\mu$ all vanish, in which case Eqs. (14)–(16) reduce to:

$$\int_\Omega \frac{\partial \phi}{\partial t} q dx + \int_\Omega \nabla\mu \cdot \nabla q dx = 0 \tag{17}$$

$$\int_\Omega \mu v dx - 2\int_\Omega u v dx + \int_\Omega \nabla u \cdot \nabla v dx + \int_\Omega ((\varepsilon - 1)\phi - \phi^3) v dx = 0 \tag{18}$$

$$\int_\Omega u w dx + \int_\Omega \nabla\phi \cdot \nabla w dx = 0 \tag{19}$$

Considering the high order spatial derivatives, a sufficiently small time step ($\Delta t \propto \Delta x^6$) is needed for explicit time integration (Galenko et al., 2013). To avoid this issue, we utilize an implicit mid-point formula for the time discretization as follows,

$$\int_\Omega \frac{\phi_{n+1} - \phi_n}{\Delta t} q dx + \int_\Omega \nabla \frac{\mu_{n+1} + \mu_n}{2} \cdot \nabla q dx = 0, \tag{20}$$

$$\int_\Omega \mu_{n+1} v dx - 2\int_\Omega u_{n+1} v dx + \int_\Omega \nabla u_{n+1} \cdot \nabla v dx + \int_\Omega ((\varepsilon - 1)\phi_{n+1} - \phi_{n+1}^3) v dx = 0, \tag{21}$$

$$\int_\Omega u_{n+1} w dx + \int_\Omega \nabla\phi_{n+1} \cdot \nabla w dx = 0, \tag{22}$$

where $\Delta t = t^{n+1} - t^n$, $(...)_n$ and $(...)_{n+1}$ denote the values of variables (ϕ, μ, u) at time t^n and t^{n+1}, respectively. The above formulation has been implemented on the software platform FEniCS (Logg and Wells, 2010).

The governing equations (20)–(22) are then solved in 2D space to mimic the confinement of a homogeneous flat substrate, which is not an unreasonable assumption if liquid copper is used as substrate during CVD growth. To investigate the influence of the crystallographic orientation of substrate on graphene CVD-growth, 3D simulations with a modified free energy functional that accounts for the interaction between graphene and substrate will be needed. This is left to the future work.

4. Comparison of GBs structures from PFC and CSL

We first use the PFC model to predict atomic structures of symmetric GBs and compare the resulting structures with those constructed by the CSL theory. To ensure GBs constructed by PFC are for the same grains studied by CSL, the initial condition for the PFC model is established based on the atomic structures of GBs constructed from the CSL theory, as shown in Fig. 2. Periodic boundary conditions are imposed in both the horizontal and vertical directions. Fig. 2 shows the discrete atomic positions from the CSL theory and the corresponding continuum density field used as the initial condition for the PFC model for a GB with misorientation angle of $\theta = 32.2^\circ$. The discrete atomic positions from CSL are shown in red, and the initial continuum density field for the PFC model in gray. The density field for the grain interior (ordered phase) is obtained by imposing a rotation matrix on Eq. (4), where the rotation angle corresponds to the grain misorientation angle. In general, it is relatively convenient in the PFC model to construct arbitrarily tilted GBs since grain orientations are well described by the density field after imposing a rotation matrix on Eq. (4). It has been shown that the density of GB defects strongly depends on grain misorientation but is insensitive to GB rotation (Wu and Wei, 2013). Therefore, symmetrical GBs could be considered as typical representatives among symmetrical and asymmetrical GBs with given misorientation angles.

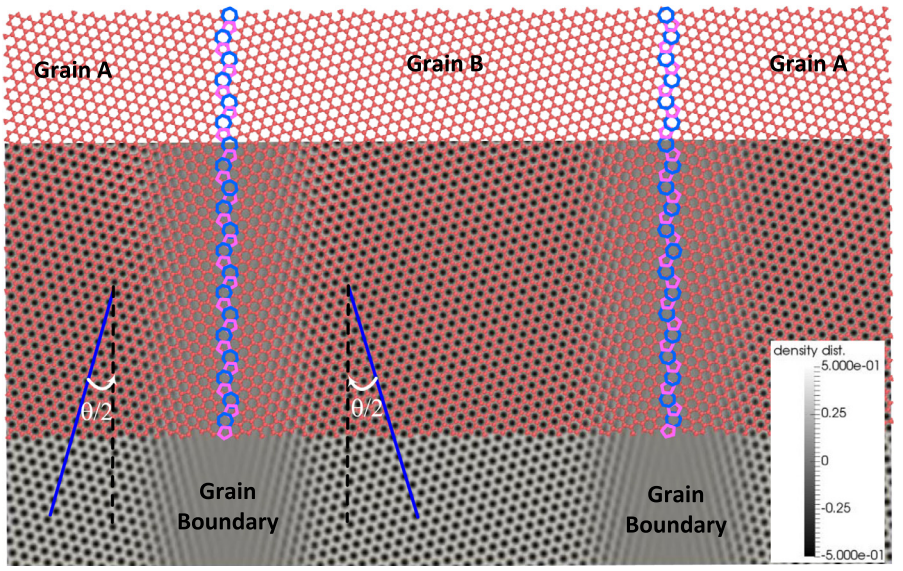

Fig. 2. Matching between the discrete atomic positions of the defected structure constructed from CSL theory (shown in red) and the continuum density distribution used as the initial condition for the PFC model (shown in gray) for a GB with $\theta = 32.2^{\circ}$. (For interpretation of the references to color in this figure legend, the reader is referred to the web version of this article.)

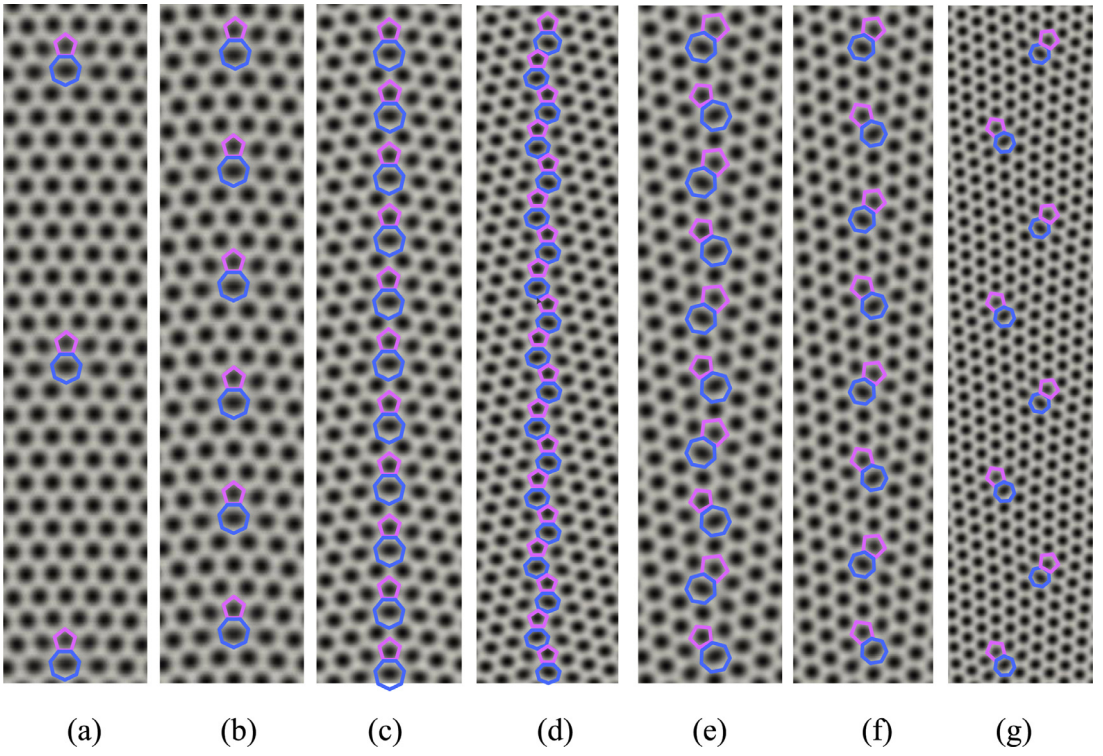

Fig. 3. Density fields predicted by the PFC model for GBs with misorientation angles of: (a) $\theta = 5.09$, (b) $\theta = 13.17$, (c) $\theta = 21.79$, (d) $\theta = 32.2$, (e) $\theta = 42.1$, (f) $\theta = 46.83$, and (g) $\theta = 50.57$.

The initial density field near the GB is taken as the average density of 0.181, analogous to a disordered liquid phase. The construction of a GB using the PFC model thus starts from a state of coexisting ordered and disordered phases, and the actual GB structure will be determined from the calculated density distribution at equilibrium. As the system reaches equilibrium, the density fields predicted by the PFC model for GBs with the same misorientation angles as those in Fig. 1 are shown in Fig. 3, where a light color denotes a high density area where atoms most likely reside. If one counts the

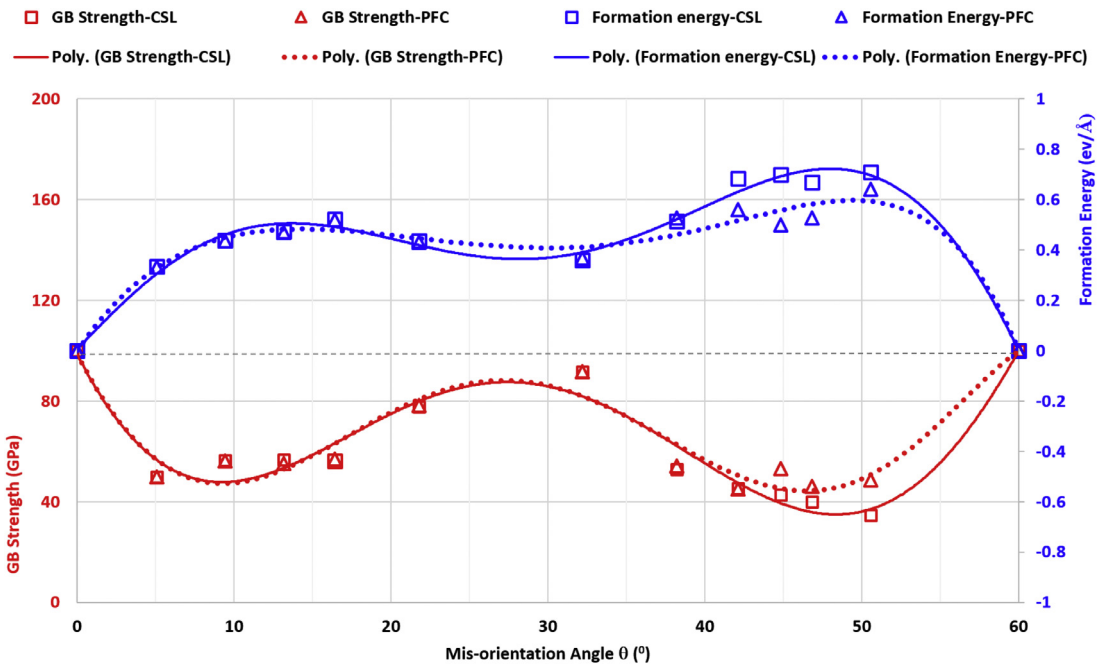

Fig. 4. Comparison of strength and formation energy of GBs constructed by CSL theory and PFC model as a function of the misorientation angle.

number of hexagons between adjacent 5|7 dislocations, it is seen that PFC simply reproduces the atomic structures from CSL for the first category of GBs by comparing Figs. 1(a–d) and 3(a–d). Symmetric GBs with misorientation angles around 20° and 32° are also observed in experiments (Ophus et al., 2015), in good agreement with our PFC result. In contrast, for the second category of GBs (Fig. 3e–g), the GB structures predicted from PFC are different from those from CSL (Fig. 1e–g). In the PFC model, the clusters of 5|7|5|7 dislocation dipoles become dispersed as the system reaches equilibrium. Similarly, the dispersed dislocations predicted from PFC have also been observed when an energy minimization method is used to construct the atomistic structures of both symmetric and asymmetric GBs (Wu and Wei, 2013).

To further understand the unexpected dispersion of 5|7|5|7 defects, MD simulations were performed via Large-scale Atomic/Molecular Massively Parallel Simulator (LAMMPS) (Plimpton, 1995) to determine the strength and formation energies of GBs constructed by CSL and PFC, as shown in Fig. 4. The interatomic force is described by the adaptive intermolecular reactive empirical bond order (AIREBO) potential (Stuart et al., 2000). Constant atom number, pressure, and temperature (NPT) ensemble is adopted in all the simulations with initial temperature of 10 K. The structure is fully relaxed before measuring the energy. The GB formation energy is calculated by subtracting the reference energy of a pristine, defect-free system from the total energy of the defected system, and then dividing the result by the length of the GB. Note that the out-of-the-plane displacement was prohibited in the calculation of GBs formation energy to mimic the substrate confinement during CVD growth. The calculated strengths and formation energies from CSL and PFC are identical for GBs in the first category, consistent with the observation that both methods lead to the same GBs structures. In contrast, for GBs in the second category, the strengths of GBs with dispersed 5|7 dislocations (constructed by PFC) are higher than those associated with clustered dislocation dipoles (constructed by CSL), and the formation energies of GBs with dispersed 5|7 dislocations (from PFC) are lower than those from CSL (up to 0.2 eV/Å for the GB with $\theta = 44.82^{\circ}$). These calculations indicate that the GB structures with clustered 5|7|5|7 dislocation dipoles predicted from CSL are not energetically favorable and should be replaced by dispersed 5|7 dislocations as predicted from PFC when building the atomic structures of corresponding GBs.

The polynomial fitting curves for the calculated GB strength and formation energy exhibit the well-known W-shape and M-shape (Fig. 4), with a local maximum strength and minimum formation energy at approximately 30°. The calculated M-shaped curve of formation energy is consistent with experimental observations of a great abundance of GBs with misorientation angles near 30° in STM images of CVD-grown graphene, as well as with the disappearance of GBs of small misorientation angles (below 15°) after sufficient thermal annealing (An et al., 2011; Huang et al., 2011; Kim et al., 2011; Yang et al., 2014).

5. PFC simulations of grain growth and GBs formation

To this date, the dynamic process of GBs formation in CVD-grown graphene still remains unclear due to a lack of effective theoretical approaches and experimental visualization methods. Understanding how GBs in graphene are formed during CVD growth is crucial to GB engineering in 2D materials, including the control of GB structure and morphology and tuning of

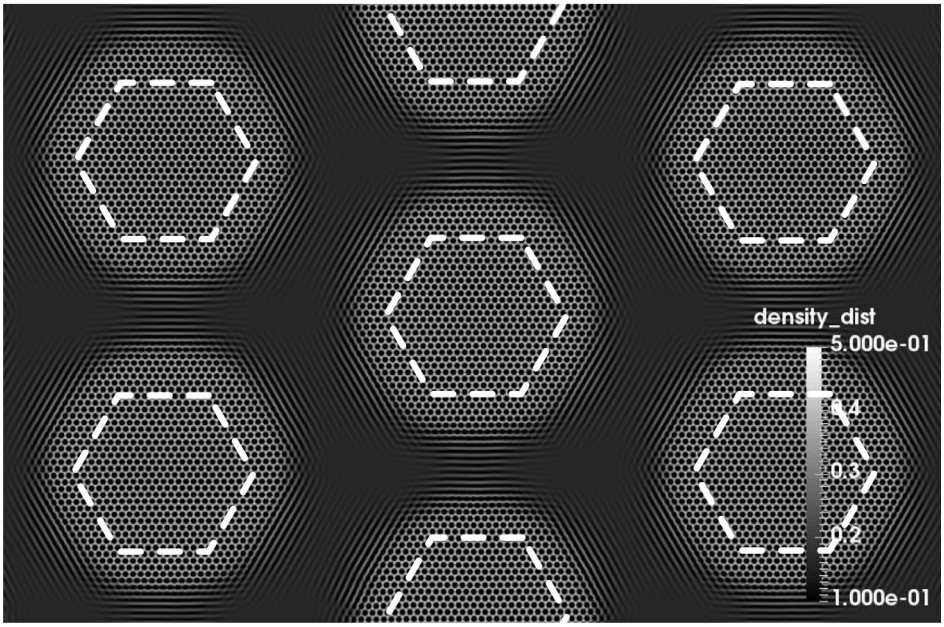

Fig. 5. Early stage of density evolution showing a hexagonal shape with zigzag dominant edges highlighted as hexagonal dashed lines.

graphene-based devices with tailor-designed properties. Intuitively, the morphology of GBs in graphene should be related to their growth protocols, which typically involve growth and coalescence of graphene islands on a substrate. PFC simulations have previously been performed to investigate the processes of grain nucleation, growth, and pattern formation during solidification of a crystalline metal from a supersaturated liquid phase (Elder et al., 2012; Tóth et al., 2010), and this approach is extended here to simulate CVD growth of 2D materials. During the CVD process, gaseous carbon atoms first aggregate to form an amorphous transitional phase surrounding the nucleated islands, and then gradually transform into ordered graphene crystals (Ago et al., 2010; Chen et al., 2010). Although the low-density gas phase is not considered in the adopted PFC model, the resulting microstructure and growth process from liquid phase to crystal phase are well captured by our model. Typical CVD-grown graphene exhibits a hexagonal shape with zig-zag edges (Gao et al., 2012; Hao et al., 2013; Ma et al., 2013; Yu et al., 2011). Fig. 5 shows a PFC simulated density evolution pattern during the early stage of island growth before grain coalescence, resembling the typical hexagonal growth of zig-zag edges during CVD (Ma et al., 2013; Wu et al., 2012). The morphology of density evolution can be controlled by the two parameters in PFC, the reduced temperature and reduced average density. The phase diagram of growth morphology associated with the two PFC parameters has been fully investigated (Tang et al., 2014) and accordingly, we chose the parameters leading to the density evolution in hexagonal shape to mimic the CVD-growth of graphene on liquid copper. With the chosen parameters, zig-zag edges possess lower interfacial energy than armchair edges (Tang et al., 2017) and therefore become the dominant edges during growth. The hexagonal dashed lines indicate the zigzag orientation of the growing islands. Here, all of the growing hexagons (and their initial seeds) have identical orientation with horizontal edges in a zigzag direction. As expected, the coalescence of islands leads to a pristine sheet of graphene with no GBs. The dynamic process of density evolution from individual islands to the steady state of a GB-free graphene is recorded in Supplementary Video 1. It is seen that grains grow hexagonally at the same growth rate due to the adopted free functional and chosen parameters in this work. The isotropic growth could be realized if a homogeneous isotropic substrate surface (such as liquid copper) is used during CVD-growth. To account for inhomogeneous CVD-growth due to the crystal orientations or defects of crystalline substrates, the free functional (Eq. (1)) should be improved by including terms capable of describing the non-uniform substrate confinements for the edge growth (Muralidharan and Haataja, 2010). This is beyond the scope of the present work.

GB engineering holds great promises for controlling physical properties of 2D materials. Seed-assisted growth has been successfully demonstrated in experiments by suppressing random nucleated islands via an array of pre-patterned seeds (Murdock et al., 2013; Song et al., 2016; Yu et al., 2011). To this date, this technique has been largely focused on identically oriented seeds with the goal of reducing GB density, and very little is known about seeds with different orientations, particularly for seeds with controlled orientations. We performed PFC simulations to demonstrate the possibility of engineering GBs morphology through controlled seeds with pre-defined locations and orientations. The simulations suggest a simple geometric rule for island coalescence, as illustrated in Fig. 6 in which five different types of engineered morphologies of GBs through pre-patterned seeds are demonstrated, where the pink color highlights the pentagon and purple color highlights the heptagon. A similar governing rule was found for the dynamic formation of GBs in CVD-grown graphene at the microscopic scale, in that the direction and misorientation angle of a GB can be determined simply from the geometries of

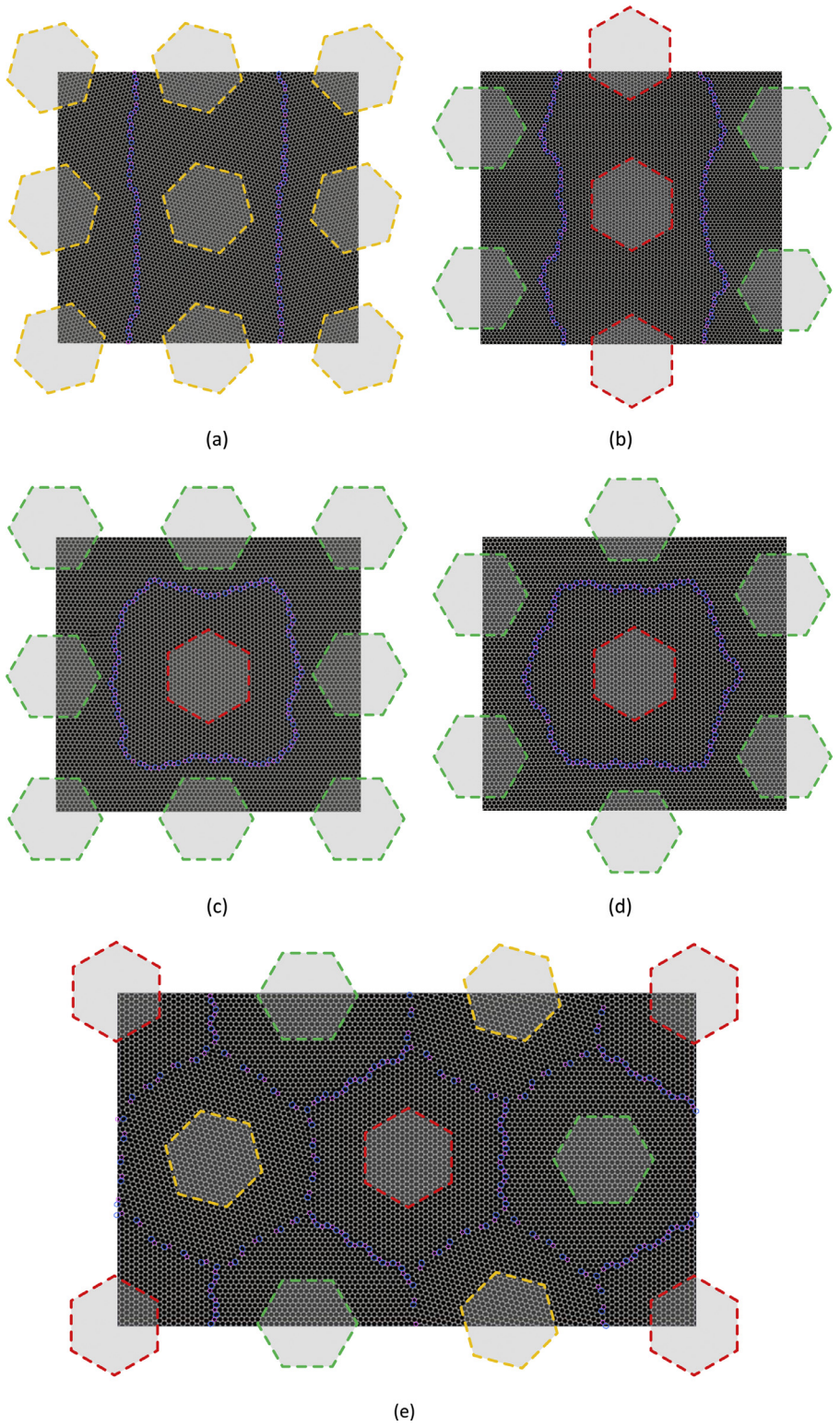

Fig. 6. GB morphologies through pre-patterned seeds: (a) straight, (b) curved, (c) square, (d) hexagonal GBs, and (e) GB network.

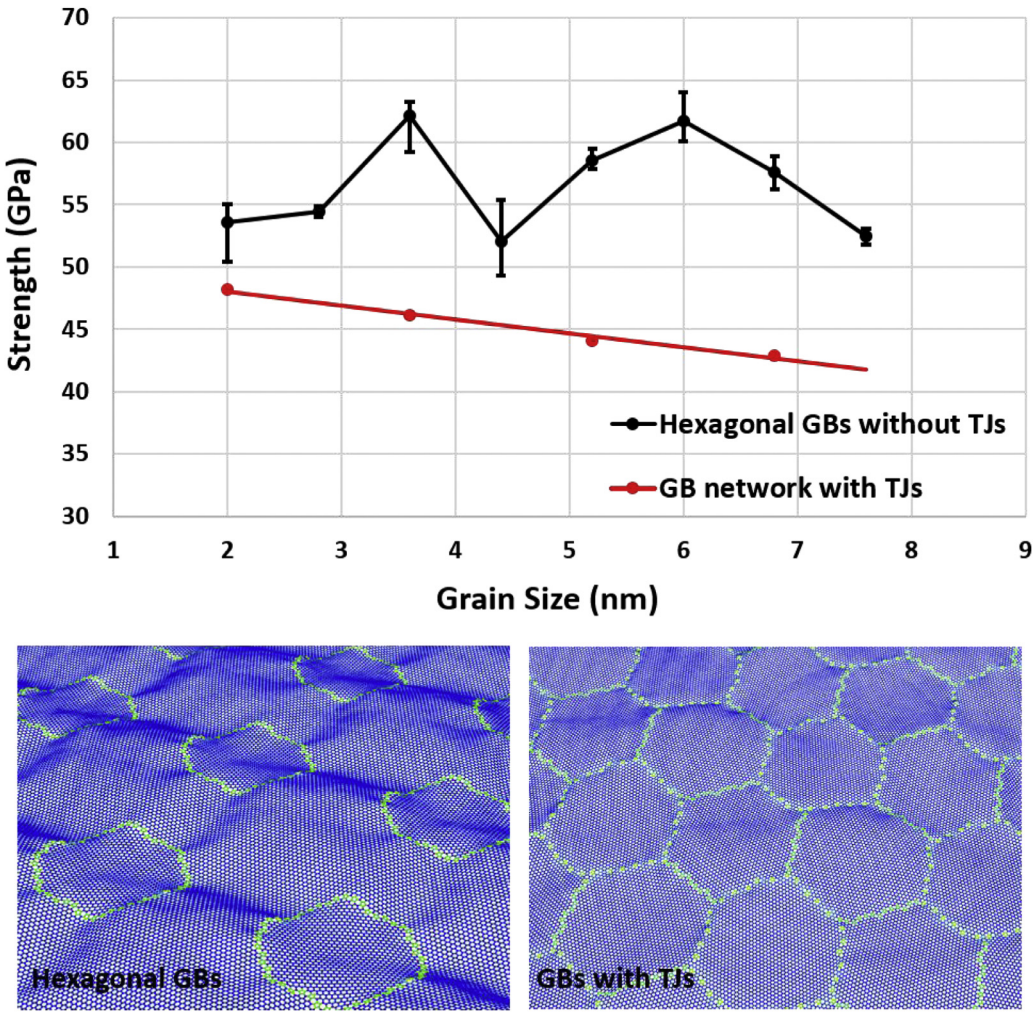

Fig. 7. Comparison of calculated mechanical strength for TJ-free graphene with hexagonal GBs and the one with TJs under biaxial tension loading for grain sizes from 2 nm to 10 nm.

polygonal graphene flakes (Guo et al., 2015). In Fig. 6(a), the growing hexagonal islands marked in yellow have a ±15° tilt angle relative to the vertical direction. As the grains are symmetrically tilted, the initial and subsequent coalescence sites stay along a straight line, leading to a nearly straight GB. In Fig. 6(b), the tilt angles of growing hexagons highlighted in green and red are 0° and 30°, respectively, leading to asymmetric growth towards a curved GB. This is consistent with the common observations of serpentine GBs (as opposed to straight ones) in experiments where the nucleation sites are often random.

As a prominent example of application for our PFC method, we explore if it is possible to grow TJ-free polycrystalline graphene through seed-controlled CVD growth. TJs are widely observed in CVD-grown graphene on different substrates, including uniform hexagonal graphene flakes grown on liquid copper (Geng et al., 2012). Depending on applications, the existence of TJs may or may not be desirable. For example, a pseudo Hall-Petch effect has been observed and attributed to the existence of TJs (Song et al., 2013). Fig. 6(c and d) shows that TJ-free graphene can be grown through proper seed control. As expected, one growing hexagon in red (30° tilted) surrounded by eight growing hexagons in green (0° tilted) leads to a square array of closed GBs without TJs (Fig. 6c), while a growing hexagon in red (30° tilted) surrounded by six growing hexagons in green (0° tilted) as nearest neighbors leads to a hexagonal arrays of closed GBs without TJs (Fig. 6d). On the other hand, seeds with all three orientations arranged in a triangle pattern produce a hexagonal GB network with TJs connecting three grains with orientations of 0°, 15°, and 30°, as shown in Fig. 6(e). In general, randomly oriented growing islands are expected to result in GBs with TJs. The dynamic processes for GBs formation in all these cases are recorded in Supplementary Videos 2–5. It can be seen that, during formation, the GB morphologies are primarily determined by the locations and orientations of pre-patterned seeds, with variations in local curvature to minimize GB energy.

It will be particularly interesting to further explore the mechanical and physical properties of TJ-free graphene. Here we only demonstrate a unique mechanical property of TJ-free graphene. Fig. 7 shows a comparison of the calculated mechanical

strength for TJ-free graphene with hexagonal GBs (assembled from the unit cell shown in Fig. 6d) and the one with TJs (assembled from the unit cell shown in Fig. 6e) under biaxial tension, as a function of grain size from 2 nm to 8 nm. Here the grain size is defined as the edge length of the hexagonal GB. In the case of TJ-free graphene, for each grain size, five samples with different distances (300–500% of grain size) between two adjacent interior grains are studied, where the average values are denoted by the solid line and maximum/minimum values are plotted as error bars. The mechanical strength of TJ-free graphene, which varies from 50 GPa to 60 GPa, is notably higher than that of graphene with TJs. Interestingly, the traditional Hall-Petch relation for polycrystalline materials is observed for GBs with TJs (red line) but not for closed GBs in TJ-free graphene (black line). A possible explanation of this phenomenon is that, according to the traditional view of the Hall–Petch relation, TJs are sites of crack nucleation with stress concentration level increasing with the grain size. In this view, once the TJs are removed, the strength of material becomes insensitive to grain size, as is observed here.

6. Conclusions

In this work, a PFC model has been developed to investigate the GB structures and formation in polycrystalline graphene during CVD growth. It is found that GBs consisting of clustered 5|7|5|7 dislocation dipoles constructed by the conventional CSL method are not energetically favorable compared to those with dispersed 5|7 dislocations predicted from the PFC model. The PFC model was used to simulate the dynamic process of pre-seeded grain growth and coalescence in CVD-grown graphene. The results suggest a simple geometrical rule that explains the dominance of curved GBs observed in experiments. As a prominent example of potential application of the developed PFC method, we demonstrate a simulation-based design of triple-junction-free polycrystalline graphene which exhibits enhanced mechanical strength and defies the traditional Hall-Petch relation. Our study may provide a potential modeling tool for GB engineering in graphene and other 2D materials.

Supporting information Five animations demonstrating PFC simulations of the dynamic process of pre-seeded graphene growth are provided as supporting materials, one for the case of all grains having the same orientation, and the rest for engineering GBs through controlled seed growth (as seen in Fig. 7).

Acknowledgments

This work has been supported by NSF under grant CMMI-1634492. The simulations reported were performed on resources provided by the Extreme Science and Engineering Discovery Environment (XSEDE) through grant MSS090046. J.L. also acknowledges support from a Hibbitt Engineering Postdoctoral Fellowship at Brown University.

Supplementary materials

Supplementary material associated with this article can be found, in the online version, at doi:10.1016/j.jmps.2017.12.013.

References

Ago, H., Ito, Y., Mizuta, N., Yoshida, K., Hu, B., Orofeo, C.M., Tsuji, M., Ikeda, K.-I., Mizuno, S., 2010. Epitaxial chemical vapor deposition growth of single-layer graphene over cobalt film crystallized on sapphire. ACS Nano 4, 7407–7414.

An, J., Voelkl, E., Suk, J.W., Li, X., Magnuson, C.W., Fu, L., Tiemeijer, P., Bischoff, M., Freitag, B., Popova, E., Ruoff, R.S., 2011. Domain (grain) boundaries and evidence of "Twinlike" structures in chemically vapor deposited grown graphene. ACS Nano 5, 2433–2439.

Artyukhov, V.I., Hao, Y., Ruoff, R.S., Yakobson, B.I., 2015. Breaking of symmetry in graphene growth on metal substrates. Phys. Rev. Lett. 114, 115502.

Backofen, R., Rätz, A., Voigt, A., 2007. Nucleation and growth by a phase field crystal (PFC) model. Philos. Mag. Lett. 87, 813–820.

Bergvall, A., Carlsson, J.M., Löfwander, T., 2015. Influence of [0001] tilt grain boundaries on the destruction of the quantum Hall effect in graphene. Phys. Rev. B 91, 245425.

Carlsson, J.M., Ghiringhelli, L.M., Fasolino, A., 2011. Theory and hierarchical calculations of the structure and energetics of [0001] tilt grain boundaries in graphene. Phys. Rev. B 84, 165423.

Chen, H., Zhu, W., Zhang, Z., 2010. Contrasting behavior of carbon nucleation in the initial stages of graphene epitaxial growth on stepped metal surfaces. Phys. Rev. Lett. 104, 186101.

Chen, L.-Q., 2002. Phase-field models for microstructure evolution. Annu. Rev. Mater. Res. 32, 113–140.

Elder, K., Grant, M., 2004. Modeling elastic and plastic deformations in nonequilibrium processing using phase field crystals. Phys. Rev. E 70, 051605.

Elder, K., Provatas, N., Berry, J., Stefanovic, P., Grant, M., 2007. Phase-field crystal modeling and classical density functional theory of freezing. Phys. Rev. B 75, 064107.

Elder, K., Rossi, G., Kanerva, P., Sanches, F., Ying, S., Granato, E., Achim, C., Ala-Nissila, T., 2012. Patterning of heteroepitaxial overlayers from nano to micron scales. Phys. Rev. Lett. 108, 226102.

Elder, K.R., Katakowski, M., Haataja, M., Grant, M., 2002. Modeling elasticity in crystal growth. Phys. Rev. Lett. 88, 245701.

Emmerich, H., Löwen, H., Wittkowski, R., Gruhn, T., Tóth, G.I., Tegze, G., Gránásy, L., 2012. Phase-field-crystal models for condensed matter dynamics on atomic length and diffusive time scales: an overview. Adv. Phys. 61, 665–743.

Galenko, P., Gomez, H., Kropotin, N., Elder, K., 2013. Unconditionally stable method and numerical solution of the hyperbolic phase-field crystal equation. Phys. Rev. E 88, 013310.

Gao, L., Ren, W., Xu, H., Jin, L., Wang, Z., Ma, T., Ma, L.-P., Zhang, Z., Fu, Q., Peng, L.-M., Bao, X., Cheng, H.-M., 2012. Repeated growth and bubbling transfer of graphene with millimetre-size single-crystal grains using platinum. Nat. Commun. 3, 699.

Gargiulo, F., Yazyev, O.V., 2013. Topological aspects of charge-carrier transmission across grain boundaries in graphene. Nano Lett. 14, 250–254.

Geng, D., Wu, B., Guo, Y., Huang, L., Xue, Y., Chen, J., Yu, G., Jiang, L., Hu, W., Liu, Y., 2012. Uniform hexagonal graphene flakes and films grown on liquid copper surface. Proc. Natl. Acad. Sci. 109, 7992–7996.

Greenwood, M., Provatas, N., Rottler, J., 2010. Free energy functionals for efficient phase field crystal modeling of structural phase transformations. Phys. Rev. Lett. 105, 045702.

Guo, W., Wu, B., Li, Y., Wang, L., Chen, J., Chen, B., Zhang, Z., Peng, L., Wang, S., Liu, Y., 2015. Governing rule for dynamic formation of grain boundaries in grown graphene. ACS Nano 9, 5792–5798.
Hao, Y., Bharathi, M., Wang, L., Liu, Y., Chen, H., Nie, S., Wang, X., Chou, H., Tan, C., Fallahazad, B., 2013. The role of surface oxygen in the growth of large single-crystal graphene on copper. Science 342, 720–723.
Hirvonen, P., Ervasti, M.M., Fan, Z., Jalalvand, M., Seymour, M., Vaez Allaei, S.M., Provatas, N., Harju, A., Elder, K.R., Ala-Nissila, T., 2016. Multiscale modeling of polycrystalline graphene: A comparison of structure and defect energies of realistic samples from phase field crystal models. Phys. Rev. B 94, 035414.
Huang, P.Y., Ruiz-Vargas, C.S., van der Zande, A.M., Whitney, W.S., Levendorf, M.P., Kevek, J.W., Garg, S., Alden, J.S., Hustedt, C.J., Zhu, Y., 2011. Grains and grain boundaries in single-layer graphene atomic patchwork quilts. Nature 469, 389–392.
Jaatinen, A., Ala-Nissila, T., 2010. Extended phase diagram of the three-dimensional phase field crystal model. J. Phys.: Condens. Matter 22, 205402.
Jauregui, L.A., Cao, H., Wu, W., Yu, Q., Chen, Y.P., 2011. Electronic properties of grains and grain boundaries in graphene grown by chemical vapor deposition. Solid State Commun. 151, 1100–1104.
Jhon, Y.I., Chung, P.S., Smith, R., Min, K.S., Yeom, G.Y., Jhon, M.S., 2013. Grain boundaries orientation effects on tensile mechanics of polycrystalline graphene. RSC Adv. 3, 9897–9903.
Jung, G., Qin, Z., Buehler, M.J., 2015. Molecular mechanics of polycrystalline graphene with enhanced fracture toughness. Extreme Mech. Lett. 2, 52–59.
Kim, K., Lee, Z., Regan, W., Kisielowski, C., Crommie, M., Zettl, A., 2011. Grain boundary mapping in polycrystalline graphene. ACS Nano 5, 2142–2146.
Kotakoski, J., Meyer, J.C., 2012. Mechanical properties of polycrystalline graphene based on a realistic atomistic model. Phys. Rev. B 85, 195447.
Lee, G.-H., Cooper, R.C., An, S.J., Lee, S., van der Zande, A., Petrone, N., Hammerberg, A.G., Lee, C., Crawford, B., Oliver, W., 2013. High-strength chemical-vapor–deposited graphene and grain boundaries. Science 340, 1073–1076.
Li, X., Cai, W., An, J., Kim, S., Nah, J., Yang, D., Piner, R., Velamakanni, A., Jung, I., Tutuc, E., 2009. Large-area synthesis of high-quality and uniform graphene films on copper foils. Science 324, 1312–1314.
Li, X., Magnuson, C.W., Venugopal, A., Tromp, R.M., Hannon, J.B., Vogel, E.M., Colombo, L., Ruoff, R.S., 2011. Large-area graphene single crystals grown by low-pressure chemical vapor deposition of methane on copper. J. Am. Chem. Soc. 133, 2816–2819.
Liu, Y., Yakobson, B.I., 2010. Cones, pringles, and grain boundary landscapes in graphene topology. Nano Lett. 10, 2178–2183.
Logg, A., Wells, G.N., 2010. DOLFIN: automated finite element computing. ACM Trans. Math. Software (TOMS) 37, 20.
Ma, C., Sun, H., Zhao, Y., Li, B., Li, Q., Zhao, A., Wang, X., Luo, Y., Yang, J., Wang, B., 2014. Evidence of van Hove singularities in ordered grain boundaries of graphene. Phys. Rev. Lett. 112, 226802.
Ma, T., Liu, Z., Wen, J., Gao, Y., Ren, X., Chen, H., Jin, C., Ma, X.-L., Xu, N., Cheng, H.-M., Ren, W., 2017. Tailoring the thermal and electrical transport properties of graphene films by grain size engineering. Nat. Commun. 8, 14486.
Ma, T., Ren, W., Zhang, X., Liu, Z., Gao, Y., Yin, L.-C., Ma, X.-L., Ding, F., Cheng, H.-M., 2013. Edge-controlled growth and kinetics of single-crystal graphene domains by chemical vapor deposition. Proc. Natl. Acad. Sci. 110, 20386–20391.
Marconi, U.M.B., Tarazona, P., 1999. Dynamic density functional theory of fluids. J. Chem. Phys. 110, 8032–8044.
Meca, E., Lowengrub, J., Kim, H., Mattevi, C., Shenoy, V.B., 2013. Epitaxial graphene growth and shape dynamics on copper: phase-field modeling and experiments. Nano Lett. 13, 5692–5697.
Mkhonta, S.K., Elder, K.R., Huang, Z.-F., 2013. Exploring the complex world of two-dimensional ordering with three modes. Phys. Rev. Lett. 111, 035501.
Mortazavi, B., Pötschke, M., Cuniberti, G., 2014. Multiscale modeling of thermal conductivity of polycrystalline graphene sheets. Nanoscale 6, 3344–3352.
Muralidharan, S., Haataja, M., 2010. Phase-field crystal modeling of compositional domain formation in ultrathin films. Phys. Rev. Lett. 105, 126101.
Murdock, A.T., Koos, A., Britton, T.B., Houben, L., Batten, T., Zhang, T., Wilkinson, A.J., Dunin-Borkowski, R.E., Lekka, C.E., Grobert, N., 2013. Controlling the orientation, edge geometry, and thickness of chemical vapor deposition graphene. ACS Nano 7, 1351–1359.
Nemes-Incze, P., Vancsó, P., Osváth, Z., Márk, G.I., Jin, X., Kim, Y.-S., Hwang, C., Lambin, P., Chapelier, C., PéterBiró, L., 2013. Electronic states of disordered grain boundaries in graphene prepared by chemical vapor deposition. Carbon 64, 178–186.
Ophus, C., Shekhawat, A., Rasool, H., Zettl, A., 2015. Large-scale experimental and theoretical study of graphene grain boundary structures. Phys. Rev. B 92, 205402.
Plimpton, S., 1995. Fast parallel algorithms for short-range molecular dynamics. J. Comput. Phys. 117, 1–19.
Provatas, N., Elder, K., 2011. Phase-Field Methods in Materials Science and Engineering. John Wiley & Sons.
Rasool, H.I., Ophus, C., Zhang, Z., Crommie, M.F., Yakobson, B.I., Zettl, A., 2014. Conserved atomic bonding sequences and strain organization of graphene grain boundaries. Nano Lett. 14, 7057–7063.
Salvalaglio, M., Backofen, R., Voigt, A., Elder, K.R., 2017. Controlling the energy of defects and interfaces in the amplitude expansion of the phase-field crystal model. Phys. Rev. E 96, 023301.
Serov, A.Y., Ong, Z.-Y., Pop, E., 2013. Effect of grain boundaries on thermal transport in graphene. Appl. Phys. Lett. 102, 033104.
Seymour, M., Provatas, N., 2016. Structural phase field crystal approach for modeling graphene and other two-dimensional structures. Phys. Rev. B 93, 035447.
Shekhawat, A., Ritchie, R.O., 2016. Toughness and strength of nanocrystalline graphene. Nat. Commun. 7, 10546.
Song, X., Gao, T., Nie, Y., Zhuang, J., Sun, J., Ma, D., Shi, J., Lin, Y., Ding, F., Zhang, Y., Liu, Z., 2016. Seed-assisted growth of single-crystalline patterned graphene domains on hexagonal boron nitride by chemical vapor deposition. Nano Lett. 16, 6109–6116.
Song, Z., Artyukhov, V.I., Yakobson, B.I., Xu, Z., 2013. Pseudo Hall–Petch strength reduction in polycrystalline graphene. Nano Lett. 13, 1829–1833.
Stuart, S.J., Tutein, A.B., Harrison, J.A., 2000. A reactive potential for hydrocarbons with intermolecular interactions. J. Chem. Phys. 112, 6472–6486.
Taha, D., Mkhonta, S., Elder, K., Huang, Z.-F., 2017. Grain boundary structures and collective dynamics of inversion domains in binary two-dimensional materials. Phys. Rev. Lett. 118, 255501.
Tang, S., Wang, J., Li, J., Wang, Z., Guo, Y., Guo, C., Zhou, Y., 2017. Phase-field-crystal investigation of the morphology of a steady-state dendrite tip on the atomic scale. Phys. Rev. E 95, 062803.
Tang, S., Yu, Y.-M., Wang, J., Li, J., Wang, Z., Guo, Y., Zhou, Y., 2014. Phase-field-crystal simulation of nonequilibrium crystal growth. Phys. Rev. E 89, 012405.
Tóth, G.I., Tegze, G., Pusztai, T., Tóth, G., Gránásy, L., 2010. Polymorphism, crystal nucleation and growth in the phase-field crystal model in 2D and 3D. J. Phys.: Condens. Matter 22, 364101.
Tsen, A.W., Brown, L., Levendorf, M.P., Ghahari, F., Huang, P.Y., Havener, R.W., Ruiz-Vargas, C.S., Muller, D.A., Kim, P., Park, J., 2012. Tailoring electrical transport across grain boundaries in polycrystalline graphene. Science 336, 1143–1146.
Wei, Y., Wu, J., Yin, H., Shi, X., Yang, R., Dresselhaus, M., 2012. The nature of strength enhancement and weakening by pentagon–heptagon defects in graphene. Nat. Mater. 11, 759–763.
Wu, J., Wei, Y., 2013. Grain misorientation and grain-boundary rotation dependent mechanical properties in polycrystalline graphene. J. Mech. Phys. Solids 61, 1421–1432.
Wu, K.-A., Plapp, M., Voorhees, P.W., 2010. Controlling crystal symmetries in phase-field crystal models. J. Phys.: Condens. Matter 22, 364102.
Wu, Y.A., Fan, Y., Speller, S., Creeth, G.L., Sadowski, J.T., He, K., Robertson, A.W., Allen, C.S., Warner, J.H., 2012. Large single crystals of graphene on melted copper using chemical vapor deposition. ACS Nano 6, 5010–5017.
Yang, B., Xu, H., Lu, J., Loh, K.P., 2014. Periodic grain boundaries formed by thermal reconstruction of polycrystalline graphene film. J. Am. Chem. Soc. 136, 12041–12046.
Yasaei, P., Fathizadeh, A., Hantehzadeh, R., Majee, A.K., El-Ghandour, A., Estrada, D., Foster, C., Aksamija, Z., Khalili-Araghi, F., Salehi-Khojin, A., 2015. Bimodal phonon scattering in graphene grain boundaries. Nano Lett. 15, 4532–4540.
Yazyev, O.V., Chen, Y.P., 2014. Polycrystalline graphene and other two-dimensional materials. Nat. Nanotechnol. 9, 755–767.
Yazyev, O.V., Louie, S.G., 2010. Electronic transport in polycrystalline graphene. Nat. Mater. 9, 806–809.

Yin, L.-J., Qiao, J.-B., Wang, W.-X., Chu, Z.-D., Zhang, K.F., Dou, R.-F., Gao, C.L., Jia, J.-F., Nie, J.-C., He, L., 2014. Tuning structures and electronic spectra of graphene layers with tilt grain boundaries. Phys. Rev. B 89, 205410.
Yu, Q., Jauregui, L.A., Wu, W., Colby, R., Tian, J., Su, Z., Cao, H., Liu, Z., Pandey, D., Wei, D., 2011. Control and characterization of individual grains and grain boundaries in graphene grown by chemical vapour deposition. Nat. Mater. 10, 443–449.
Zhang, H., Lee, G., Fonseca, A.F., Borders, T.L., Cho, K., 2010. Isotope effect on the thermal conductivity of graphene. J. Nanomater. 2010, 7.
Zhang, J., Zhao, J., 2013. Structures and electronic properties of symmetric and nonsymmetric graphene grain boundaries. Carbon 55, 151–159.
Zhang, T., Li, X., Gao, H., 2014. Designing graphene structures with controlled distributions of topological defects: a case study of toughness enhancement in graphene ruga. Extreme Mech. Lett. 1, 3–8.
Zhang, Z., Yang, Y., Xu, F., Wang, L., Yakobson, B.I., 2015. Unraveling the sinuous grain boundaries in graphene. Adv. Funct. Mater. 25, 367–373.
Zhuang, J., Zhao, R., Dong, J., Yan, T., Ding, F., 2016. Evolution of domains and grain boundaries in graphene: a kinetic Monte Carlo simulation. Phys. Chem. Chem. Phys. 18, 2932–2939.